Clinical Applications of Dynamic Optical Tomography In Vascular Disease

Gregg S. Landis MD[1], Thomas F. Panetta MD[1], Seth B. Blattman MD[1], Harry L. Graber PhD[2],
Yaling Pei PhD[2], Christoph H. Schmitz PhD[2], and Randall L. Barbour PhD[2]

[1]Department of Vascular Surgery and [2]Department of Pathology
SUNY Downstate Medical Center, Brooklyn, New York 11203

1. ABSTRACT

Vascular disease is a significant source of mortality and morbidity for many patient populations. While substantial strides in surgical therapeutics have been made in the past decade, our limited understanding of the microvascular processes, which are invisible to conventional imaging modalities and beyond the scope of our current physiologic paradigms, has slowed the advancement of medical therapeutic interventions. In this report we present data in support of an emerging body of work demonstrating that the method of dynamic optical tomography can yield critical insights into the underpinnings of microvascular pathophysiology in large tissue structures. In a series of experiments designed to characterize specific properties of the peripheral vasculature, we provide first–time descriptions of spatially mapped time–varying vascular responses. Specifically, properties delineated are (1) that inherent vascular rhythms can act as natural "contrast agents" that allow spatial discrimination of tissue components in cross–section, (2) that complex vascular responses can be decomposed into multiple spatially coincident time–evolving processes, and (3) that occult long–term "evolutionary–type" microvascular processes (*e.g.*, chronic tobacco use) can be revealed. Taken together, these capabilities contribute to a global understanding of the peripheral vascular response, affording new opportunities for improved diagnostic and therapeutic strategies.

2. INTRODUCTION

Clinical manifestations of disease states are the aggregate response of diverse tissue types to insult. As is the case with all specialized tissues, the vasculature's response to insult, or to other forms of stimulation, is constrained to a series of specialized responses commonly referred to as vascular reactivity. It is convenient to consider these as occurring on both micro– and macrovascular scale. Examples of microvascular responses are changes in gas and nutrient exchange, platelet aggregation, thrombus formation, luminal remodeling, and elaboration of autoregulatory mediators.[1,2] On the macrovascular scale, vasodilatation, vasoconstriction, and shunting of blood via arteriovenous communications are typical responses. Because of the sensitive dependence of all tissues on their local vascular supply, the tissue–vascular interface is ultimately the focal point of any investigation of disease processes. It follows that the specific characteristics of the tissue–vascular interaction can be a signature of disease processes. While this principle is generally understood, detection of these signatures in large tissue structures using noninvasive methods has been elusive.

By means of argument and experimental findings, in this report we present evidence that these interactions can be detected and characterized by measures of the temporal variability in hemoglobin states. In the following section we review features of the vascular response that support both this assertion and our view that these signatures can be identified from the analysis of time–series image data collected using near infrared (NIR) tomographic imaging methods.

2.1 Spatiotemporal Features of the Vascular Response

While it is convenient to think of blood vessels as simple pipes or tubes conveying blood, it has long been apparent that the vasculature is a complete organ system. Like other organ systems, the vasculature is capable of dynamically reacting to a multitude of intravascular and extravascular stimuli. These stimuli induce vascular responses that are both spatially and temporally varying, and occur over a range of time scales. The details of these responses are thought to reflect the dynamic interaction between the blood, vascular endothelium, and the specific end organ (*i.e.*, the tissue–vascular interface).

The vascular tree is anatomically and functionally spatially heterogeneous. Anatomic heterogeneity arises from the existence of a spectrum of vessel types, vessel calibers, and large–scale architectural features. This heterogeneity has evolved to provide an arborizing network of vessels to optimally perfuse distant tissue beds. Structurally, this network is composed of three broad categories of vessels — arteries, microvessels, and veins — that all have distinct histologic and functional

characteristics. Functionally, while large and medium–sized arteries and veins serve as conduits for blood flow, the microvessels constitute the interface where tissue–vascular coupling occurs.

Accompanying this structural–functional heterogeneity is the occurrence of natural beat frequencies that are mediated by local and central control mechanisms. The cardiac beat frequency is the result of a systolic/diastolic pressure wave initiated at the left ventricle. It has its greatest amplitude in the proximal arterial tree. The respiratory beat frequency is seen throughout the venous side of the circulation. It is well appreciated that changes in intrathoracic pressure attributable to the respiratory cycle are transmitted to the periphery primarily as time–dependent variations in venous return. This generates a respiratory beat frequency, observable in all post–capillary vessels, whose magnitude decreases with increasing distance from the chest. Vasomotion is caused by local autoregulatory responses, and results in rhythmic small vessel vasodilatation or vasoconstriction.[3,4] These natural beat frequencies found in flowing blood, result in subtle yet measurable fluctuations in tissue hemoglobin volume.

In addition to the occurrence of these natural beat–to–beat rhythms, the vascular response occurs across multiple time scales. Here we categorize these into four time frames: beat–to–beat variations, immediate responses to provocation, short–term responses to provocation, and long–term evolutionary changes from chronic disease processes.

The first order of time–scale is the aforementioned beat–to–beat variation. These are generally phenomena that occur over a brief time period, often within the time span of a single cardiac cycle. Careful examination of these rhythms has served to identify the existence of control mechanisms masked by the occurrence of chaotic or other complex behaviors.[5] The next order of time scale is the immediate response to provocation. Examples of these include the vascular response to nerve activation caused by evoked sensory, motor or cognitive stimuli,[6] response to a fast–acting drug, or the response caused by alteration in blood flow produced by, for instance, a pneumatic tourniquet. These responses typically occur over several seconds to minutes. Examination of these can reveal sufficiency of tissue reserves or the adequacy of other functional processes associated with the mediating stimulus. The next time scale is the short–term response that occurs over hours to days. These can be produced in response to acute disease processes or reflect the prolonged influence of a pharmacological agent. Last are time scales that reflect long–term "evolutionary type" changes spanning years to decades, as a consequence of chronic disease.

2.2 Functional Imaging of the Vascular Response by Dynamic Optical Tomography

While the above phenomenology is generally appreciated, at least by those who specialize in the clinical management of vascular disease, what is not evident is the nature of the information that can be derived by studying the *temporal* characteristics of the vascular response using continuous, fast NIR imaging methods. From what we can currently see, the attainable information falls into three categories. One type of information is a spatial map of particular components of the vascular tree. An example of this is the results shown below, where major subsurface veins can be delineated within the cross section by the presence of a dominant respiratory beat frequency. Another type of information is the mapping of functional responses to provocation. By example, we have studied the vascular response of the forearm to arterial occlusion. It can be expected that global provocations of this sort will produce a complex vascular response whose details reflect a cascade of events occurring at the tissue–vascular interface. Significantly, this information can be decomposed, seemingly for the first time, to allow assignment of functional responses to discrete anatomical sites. In effect, the temporal evolution of the vascular response can be imaged. Naturally, provocations can take on many forms, ranging from simple local manipulations (*e.g.*, use of a pneumatic tourniquet) to complex systemic stimuli. We are currently testing the feasibility of the detection of breast tumors by examining the vascular response to provocation. An altered response can be expected, owing to the known ultrastructural and functional derangements that exist in tumor angiogenesis. Similarly, other types of disease processes might be discernible by examining the response to provocation. By example, we illustrate an attenuated vascular response caused by chronic tobacco use.

The third type of information we believe can be defined comes from use of more sophisticated feature–extraction methods. Similar to the dynamics of other naturally occurring processes (*e.g.*, heart–rate variability[7]), classification of specific functional forms of the temporal response (*e.g.*, chaotic behavior) may serve to improve early disease detection and monitoring (see accompanying reports by Barbour *et al.*[8] and Graber *et al.*[9]).

While the ultimate clinical utility of the above measures is yet to be demonstrated, it deserves emphasis that all of the above information can be derived without the use of contrast agents. In effect, our "contrast agent" is the naturally occurring or induced temporal properties of the vasculature itself.

3. MATERIALS AND METHODS

3.1 Experimental Design

All subjects involved in this report were male volunteers aged 28 to 45 (mean 36.4). All subjects were healthy non–smokers (with the exception of the experiment evaluating chronic tobacco use), without known diabetes mellitus, coronary artery disease, hypertension, or peripheral vascular disease. All were found to have unremarkable physical exams. Subjects placed either forearm into the circular fiber–optic limb–measuring head, and made contact directly with the co–located source and detector fibers, approximately 5–8 cm proximal to the wrist. During each experiment, the subject was asked either to perform a series of respiratory maneuvers, or to undergo reduction or occlusion of brachial artery inflow, the details of which are described below.

Subjects underwent simultaneous electrocardiography to objectively measure continuous changes in heart and respiratory rates. The experimental protocol and informed consent were approved by the Institutional Review Board of the medical center. All subjects gave informed consent prior to participation.

3.1.1 Beat–to–beat variation in optical contrast from natural vascular rhythms.

In this series of experiments, subjects were instructed to maximally inhale and exhale with each respiratory cycle. A metronome was provided to encourage regular rhythmic breathing.

3.1.2 Immediate Response to Provocation: Reactive Hyperemia

In this series of experiments, subjects placed either arm into the limb–measuring head, and a pneumatic tourniquet was applied to the upper arm. The protocol involved a period of basal measurement (1 minute), followed by application of occlusion pressure for approximately 4 minutes, with a 5–minute observation period following release of the tourniquet. During this period, full tomographic dynamic optical imaging measurements were performed at a framing rate of 3 Hz. Also recorded were changes in the patient's clinical exam (*e.g.*, visual onset of reactive hyperemia).

3.1.3 Long–term System Evolution: Effect of Chronic Tobacco Use

In this experiment, we compared the provoked vascular response, as measured by detector signal intensity, in a chronic heavy smoker and a non–smoker. Both subjects had similar forearm geometries and body habitus. Following a brief period of baseline measurement (~90 sec), 50 mmHg cuff pressure was applied to the brachial artery and maintained for ~90 sec, then released.

3.2 Data Collection

Optical measurements were performed using instrumentation described in the accompanying report by Schmitz *et al*.[10] Data were collected using a circular measuring head that made contact with the subject's forearm. Transmitting and receiving optical fibers were co–located, forming a "bull's eye" geometry with the source fiber in the center. These were uniformly spaced about the arm and included a 16–source by 16–detector measurement (256 source–detector pairs). Dynamic measurements were performed at a framing rate of approximately 3 Hz, which corresponds to a source switching speed of ~50 Hz. For each source position, light intensity measurements were performed in parallel. Depending on the experiment, the number of image frames (time points) collected varied between 750 and 1,800.

2.3 Image reconstruction

The optical inverse formulation was based on the normalized difference method,[11,12] in which the equation that we solve has the form

$$\mathbf{W}_r \delta \mathbf{x} = \delta \mathbf{I}_r \qquad (1)$$

where $\delta \mathbf{x}$ is the vector of differences between the optical properties (*e.g.*, absorption and scattering coefficients) of a target (measured) and a "background" medium, $\mathbf{W}_r$ is the weight matrix describing the influence that each voxel or element has on the surface detectors for the selected reference medium, and $\delta \mathbf{I}_r$ represents a modified difference between detector readings obtained from the target in two distinct states. The normalized difference is defined by

$$(\delta\mathbf{I}_r)_i = \frac{(\mathbf{I}-\mathbf{I}_0)_i}{(\mathbf{I}_0)_i}(\mathbf{I}_r)_i,$$ (2)

where $\mathbf{I}_r$ is the computed detector readings corresponding to a selected reference medium, and $\mathbf{I}$ and $\mathbf{I}_0$ represent two sets of measured data (*e.g.*, background *vs.* target, time–averaged mean *vs.* a specific time point, *etc.*).

For both the simulation and experimental data, image reconstructions were carried out by using a conjugate gradient descent (CGD) algorithm to compute numerical solutions to the modified perturbation equation, without imposition of any constraints or weight–matrix scaling. Quantities obtained from the "background medium" were computed using diffusion theory and employed the same source–detector geometry as that used for the target medium.

2.3 Time Series Image Analysis

To identify contrast features associated with temporal variability in optical coefficients, various standard numerical methods were used. In one instance, a spatial map of the standard deviation of the reconstructed absorption coefficient value was obtained by computing this value for the time–series image data in each pixel. In another case, a spatial map of the amplitude of the cross–spectral density (CSD) between a surface detector and the image series was computed. The CSD function G_{uv} of the time–series pair u and v is the Fourier transform of their cross–correlation function. A discrete Fourier transform computation — $U(n)$, $V(n)$, $n=1,2,\ldots,n_d$ — is carried out for each record, and the cross–spectral density estimate is

$$G_{uv}(k') = 2\sum_{n=1}^{n_d}\left[U_{k'}^R(n) - jU_{k'}^I(n)\right]\left[V_{k'}^R(n) + jV_{k'}^I(n)\right]\Big/N.$$ (3)

with $k' = 0,1,\ldots,N/(2n_d)$ for N even; $0,1,\ldots,(N-1)/(2n_d)$ for N odd. In still another case, we computed spatial maps that reveal the amplitude of the principal components of the pixel data using methods described subsequently.

2.4 Principal component analysis

For concreteness, suppose we are working with a time series of N reconstructed images of a medium's absorption coefficient μ_a, and that the medium under investigation is a section of a biological structure. The entire series can be thought of as a single mathematical function with spatial and temporal independent variables: $\mu_a(i,j,t)$, where i and j are the pixels' row and column indices, respectively. In other reports that have dealt with extraction of functional information through time–series analysis operations, such as the computation of (linear) power spectra[13] or (nonlinear) correlation dimensions,[14] we have implicitly assumed that $\mu_a(i,j,t)$ should be decomposed into a sum of time–varying functions, each one corresponding to a given spatial location. However, other representations, which are equally valid mathematically, may be preferable from an information–extraction perspective.

On the basis of known physiology, our expectation is that there is some number M of physiological rhythms present in the target medium, each of which has the effect of producing temporal fluctuations in μ_a. We will further assume that the amplitudes of these rhythms are such that the relations between the physiological parameter variations and the associated μ_a variations are effectively linear. Each of these rhythms may have a different spatial distribution across the area of the image, and M may be significantly smaller than N. If the spatial amplitude pattern of the mth physiological rhythm is denoted by $S_m(i,j)$, and the corresponding temporal fluctuation by $T_m(t)$, then the net spatiotemporal μ_a variation in the medium will be proportional to $\sum_{m=1}^{M}k_m S_m(i,j)T_m(t)$, for some particular set of constants $k_1, \ldots, k_M$. In that case, an appropriate strategy for image–series analysis is to attempt to decompose the reconstructed $\mu_a(i,j,t)$ into a set of spatial and temporal components that can be related to these underlying patterns of physiological activity. That is, one post–reconstruction analysis goal should be to solve the system of equations $\mu_a(i,j,t) = \sum_{m=1}^{M}k_m S_m(i,j)T_m(t)$ for the unknown k_ms, S_ms and T_ms.

The just–described problem has infinitely many solutions, all of which mathematically are equally correct. In general, then, it cannot be claimed with certainty that the functions that are the result of a particular decomposition computation accurately reflect the spatial or temporal physiological patterns that actually were present in the target medium. It is necessary in practice to employ some means of selecting a particular solution from the set of all possible ones. Among the ways in which this can be done are by specifying additional criteria that the solution must satisfy, or by making use of *a priori* knowledge about the spatial and/or temporal patterns that one expects to find in tissue. The technique used in this report is known as principal component analysis (PCA), which is an example of the former approach. The "additional criteria" that it imposes on the solution are: first, that the computed temporal functions be uncorrelated with each other; second, that each term in the

resulting summation account for as large a fraction of the overall variance in $\mu_a(i,j,t)$ as is possible without violating the zero–correlation requirement.

The input data for a PCA computation is a series of N reconstructed μ_a images, each with I rows and J columns of pixels. The first step is to subtract from each image its mean value: $\mu_a^*(i,j,t) = \mu_a(i,j,t) - \langle \mu_a(t) \rangle$, where $\langle \mu_a(t) \rangle$ is the time–dependent mean value of μ_a over the full area of the image. Each mean–subtracted image in the time series then is recast as a $(I \times J) \times 1$ vector. Here we use the symbol $\mathbf{a}_n$ to denote the vector corresponding to the nth image. (The only requirement for this step is that the same method of mapping image pixel locations into vector elements be used for all images in the series.) Next, the $N \times N$ matrix $\mathbf{C}$ is computed, whose $n'n''^{\text{th}}$ element is the covariance between the n'^{th} and n''^{th} mean–subtracted images in the time series: $C_{n'n''} = (N-1)^{-1} \sum_{n=1}^{N} (\mathbf{a}_{n'})_n (\mathbf{a}_{n''})_n$. The eigenvalues ($\lambda_1$, …, λ_N; by convention, these are ordered so that $\lambda_1 > \dots > \lambda_N$) and eigenvectors ($\mathbf{u}_1$, …, $\mathbf{u}_N$, with $\mathbf{u}_n$ the eigenvector corresponding to eigenvalue λ_n; by convention, $\mathbf{u}_n$ is normalized such that $\|\mathbf{u}_n\|^2 = 1$) of $\mathbf{C}$ are then computed. Each eigenvector has N elements, and so can be interpreted as a time series. Finally, a set of "eigenimages" ($\mathbf{b}_1$, …, $\mathbf{b}_N$) is generated, each of which is an average of the original N images, weighted by the elements in one of the normalized eigenvectors and by the corresponding eigenvalue, according to

$$\mathbf{b}_n = \frac{1}{\lambda_n} \left[(\mathbf{u}_n)_1 \mathbf{a}_1 + (\mathbf{u}_n)_2 \mathbf{a}_2 + \dots + (\mathbf{u}_n)_N \mathbf{a}_N \right]. \tag{4}$$

Each $\mathbf{b}_n$ is converted into a $I \times J$–pixel image, by applying the inverse of the same mapping that was used to generate the set of vectors $\{\mathbf{a}_n\}$.

The principal components essentially are a particular rearrangement of the image time series; each eigenvector is a different linear combination of the $I \times J$ individual–pixel time series, while each eigenimage is a different linear combination of the N reconstructed images. Importantly, all the information that is present in $\mu_a^*(i,j,t)$ is preserved in its principal components. To demonstrate this, we define $\mathbf{A}$, $\mathbf{B}$, and $\mathbf{U}$ as the matrices whose n^{th} columns are the vectors $\mathbf{a}_n$, $\mathbf{b}_n$ and $\mathbf{u}_n$, respectively, and $\mathbf{\Lambda}$ as the matrix whose $n'n''^{\text{th}}$ element is equal to $\lambda_{n'}\delta_{n'n''}$. From Eq. 4 it follows that $\mathbf{B} = \mathbf{\Lambda}^{-1}\mathbf{AU}$, and so $\mathbf{A} = \mathbf{\Lambda B U}^{-1}$. Then any particular element of $\mathbf{A}$ (*i.e.*, any particular value from the spatiotemporal function $\mu_a^*(i,j,t)$) can be recovered: $A_{n'n''} = \sum_{n=1}^{N} \lambda_n B_{n'n} U_{nn''}^{-1}$.

As previously mentioned, the $\mathbf{u}_n$s may be interpreted as time series. These temporal functions are uncorrelated, as a consequence of a fundamental property of symmetric matrices: eigenvectors associated with distinct eigenvalues necessarily are orthogonal.[15] While it is mathematically possible that two or more of the λ_ns that correspond to a particular $\mu_a^*(i,j,t)$ could be precisely equal, the probability of this occurring when experimental data sets are analyzed is vanishingly small. Each eigenvalue obtained in practice invariably is unique. Then, as the covariance matrix $\mathbf{C}$ is necessarily symmetric (because $\mathrm{cov}(\mathbf{a}_{n'},\mathbf{a}_{n''}) = \mathrm{cov}(\mathbf{a}_{n''},\mathbf{a}_{n'})$), each $\mathbf{u}_n$ is orthogonal to (*i.e.*, uncorrelated with) all the others.

The previously mentioned variance–maximizing property of PCA can be restated as: the set of principal components for eigenvalues λ_1 through λ_M, with $M < N$, accounts for the largest percentage of the overall spatiotemporal variance in $\mu_a^*(i,j,t)$ that can possibly be contained in any M–term sum of products of purely spatial functions and purely temporal functions. Proof of this property can be found in Ref. 16. If we denote the sum of all eigenvalues as L, then the fraction of the total variance in $\mu_a^*(i,j,t)$ that is accounted for by the nth principal component is equal to λ_n/L.[16] It frequently is found in practice that there is some number $M \ll N$ such that $\sum_{n=M+1}^{N} \lambda_n/L \ll 1$, *i.e.*, that all eigenvalues after some particular one are trivially small. This fact has both physiological and mathematical significance. Physiologically, we would expect that vascular response patterns that have large amplitude and are strongly coordinated over large volumes of tissue would give rise to principal components with large eigenvalues. In contrast, responses that have small amplitudes, or are restricted to small regions of tissue, or that primarily are the result of local metabolic control and therefore occur in a globally uncoordinated manner, would correspond to principal components with smaller eigenvalues. So too should any type of noise whose effects on the reconstructed images is spatially uncorrelated. Therefore it is appropriate to compute only the first M eigenvectors and eigenimages. Mathematically, the approximation to the matrix $\mathbf{A}$ of original (mean–subtracted) images that is obtained from the truncated PCA computation is $\mathbf{A}_M = \mathbf{\Lambda}_M \mathbf{B}_M \mathbf{U}_M^+$, where $\mathbf{\Lambda}_M$ is the $M \times M$ diagonal matrix containing the

first M eigenvalues on its main diagonal, $\mathbf{B}_M$ consists of the first M columns of $\mathbf{B}$, and $\mathbf{U}_M^+$ is the $M \times N$ pseudoinverse of $\mathbf{U}_M$: $\mathbf{U}_M^+ = \left(\mathbf{U}_M \mathbf{U}_M^T \right)^{-1} \mathbf{U}_M^T$,[15] where $\mathbf{U}_M$ consists of the first M rows of $\mathbf{U}$. Because the first M principal components account for almost all of the variance in $\mu_a^*(i, j, t)$, the difference between $\mathbf{A}$ and $\mathbf{A}_M$ is slight.

There is no guarantee that a one–to–one correspondence exists between a set of principal components and the set of physiological processes that gave rise to the observed spatiotemporal variability of $\mu_a^*(i, j, t)$ (for example, there is no *a priori* reason why the temporal patterns corresponding to the different physiological rhythms must be orthogonal). Principal components nevertheless are informative in themselves[17] and are useful as a starting point for many higher–order signal–separation algorithms.[18,19]

4. RESULTS

4.1 Beat–to–beat variation in optical contrast from natural vascular rhythms

In this study a subject was asked to regulate deep breathing by following a metronome to amplify the respiratory response. Data were collected by placing a ring of optical fibers in contact with the skin about the subject's left forearm. A total of 1,500 tomographic scans were collected over a period lasting 500 seconds. This period of time was selected into order to obtain a more representative assessment of the nature of the peripheral vascular response to deep breathing. The resulting time series of reconstructed images were then analyzed to identify, in the cross section, the time–varying features of interest.

One useful global measure of reactivity is a spatial map revealing the standard deviation of the temporal variations in the pixel data. This is shown in Figure 1. The map directly reveals the magnitude of temporal variability in the cross section and in particular shows that regions with the largest variability occur in the peripheral areas of the cross section. For instance, by carefully noting the positioning of the optical fibers, we observed that the high–amplitude region at coordinates row 8, column 15 corresponds to a large subsurface vein.

A more detailed examination of the temporal properties can be obtained by computing the frequency structure of the pixel data. We have chosen to accomplish this by computing the cross–spectral density (CSD) between a surface detector and the image pixels. This measure is similar to a power spectrum but involves two different time series. Our rationale for considering this is the expectation that detector data contains the most reliable information available from the experiment about the target. The images, on the other hand, which are derived from all detector data, almost certainly will contain some artifact originating from detector noise, modeling error, and numerical sources of various kinds. Since each image frame is computed independently of all others, it is our contention that these should not introduce any specific bias into the temporal data, and it is unlikely that any such bias would coincide with a biological frequency. Accordingly, a spatial map revealing the CSD amplitude at a chosen frequency serves to identify where in the cross section a particular frequency occurs. Figure 2 shows such a map at the frequency of regulated breathing (0.12 Hz). Comparison of this to Figure 1 shows considerable overlap,
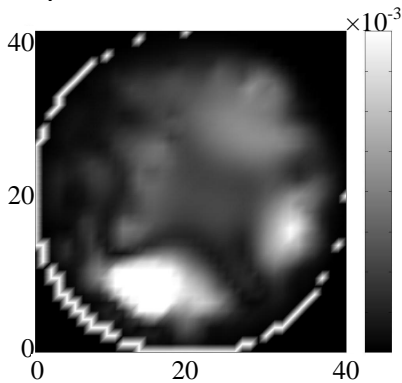
Figure 1: Standard Deviation Map
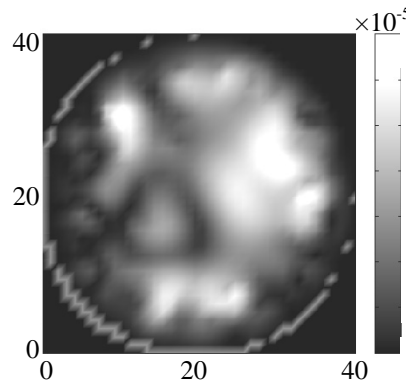
Figure 2: Cross Spectral Density Map
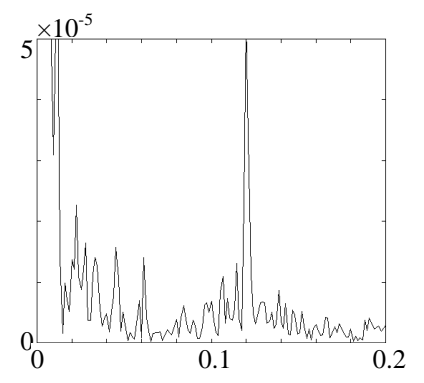
Figure 3: Plot of Cross–Spectral Density Amplitude *vs.* Frequency (Hz)

indicating that much of the observed variance in the pixel data coincides with enhanced respiratory activity. Confirmation of the existence of enhanced dynamics in response to respiratory activity is shown by the frequency spectrum shown in Figure 3. This spectrum is typical of that found in the regions shown in Figure 2 having large CSD amplitudes. In another report,

we have used similar methods to map regions in the forearm that have enhanced amplitudes at the cardiac frequency.[14] An overlay of these maps with an MRI image of the same test site showed excellent spatial agreement with the radial, interosseous and ulnar arteries.

4.2 Immediate Response to Provocation: Reactive Hyperemia

Reactive hyperemia occurs in response to iatrogenically applied transient tissue ischemia. The result is a marked erythematous response in the skin, vasodilatation, and shunting of blood to the peripheral soft tissues. This procedure is commonly invoked in various clinical situations to open tissue outflow beds in order to improve angiographic images and facilitate measuring of post–arterial reconstruction pressure gradients. Although the gross characteristics of this phenomenon are well known, the tissue–specific response to this maneuver has yet to be delineated.

To initiate the reactive hyperemic response, we temporarily occluded the brachial artery by means of a pneumatic tourniquet. Data shown in Figure 4 illustrates a typical time course of the measured light intensity collected about the arm for a single illumination site. The details of the measured response varied, depending on the chosen source location, but in all cases were grossly similar to that shown. Inspection of the time course reveals four prominent features. During the initial rest period (0–100 sec), low–frequency fluctuations due to vasomotion are apparent. A frequency analysis of the time series revealed the other expected vascular rhythms – cardiac and respiratory frequencies (not shown). Apart from these variations, the amplitude of the signal intensities is relatively constant. Inflow occlusion is marked by a rapid decrease in measured light intensity followed by a more gradual decline. These findings are consistent with venous congestion resulting from venous outflow occlusion, prior to the completion of arterial inflow occlusion. We believe that the more gradual downtrend seen is evidence of a subtle redistribution of blood within soft tissues. The latter is seen more clearly in time plots of other source locations, where for some detectors a change in the direction of the trend is seen during this period (results not shown).

Figure 4
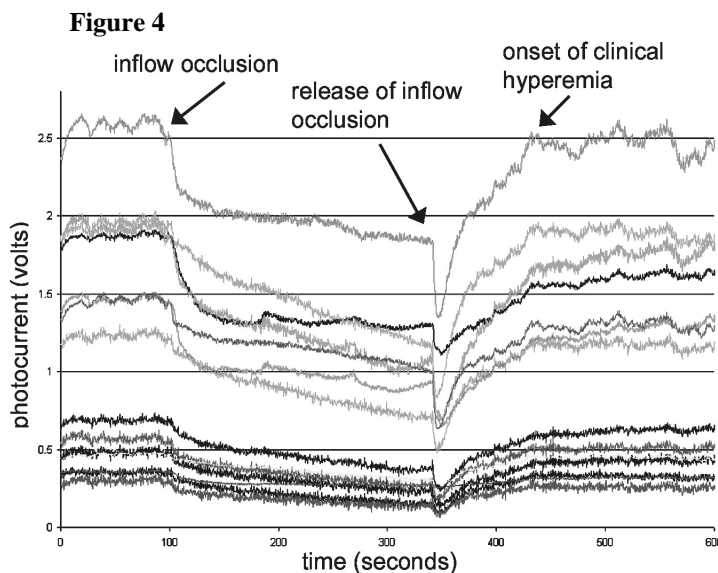
Reactive hyperemia: Detector data (single light source) demonstrating variations in signal intensity following obliteration and restoration of brachial arterial inflow. Clinical observation of tissue hyperemia was noted at 435 seconds.

A marked nadir in the detector tracings occurs at approximately 350 sec, and rapidly follows the release of the arterial inflow occlusion, but precedes full restoration of venous outflow, resulting in a transient venous hypercongestion. This is followed by a rapid increase in signal intensity, indicating net reduction in tissue blood volume. Also noted in the figure is the onset of clinical hyperemia. Visual inspection showed that this continued for approximately 30 seconds, followed by a return to normal skin pallor. The optical response to hyperemia should result in a reduction in signal intensity. For some of the detector responses shown, a modest decline in signal levels is seen. Inspection of time plots for other source positions revealed a more marked decline than shown here for certain detectors.

To further explore the vascular response to the imposed manipulation, we have analyzed the resulting image time series using the method of principal component analysis. This method is conceptually similar to a Fourier analysis, except that rather than decomposing a function into a linear combination of trigonometric functions of different frequencies, it instead

decomposes a time series into a linear sum of other time series. Within the framework of a linear system, the resultant decomposition represents the principal components of the time–varying behavior occurring, in our case, in all pixels. A spatial map revealing the amplitude of the extracted time varying behavior can be generated for each principal component. In this manner we are able to extract a complete series of time–varying behaviors that are spatially coincident. It is worth noting the approach taken here is essentially the same as used by others[17] for characterizing similar behaviors based on optical measurements from the surface of tissue. In our case, however, we are using PCA to define spatially coincident behavior in cross section. Results of this analysis are shown in Figure 5. Panel A shows the cumulative percentage of variance for the first M principal component, with $M = 1$ through 10. Inspection shows that the temporal variability described by the first component comprises nearly 60% of the total, the second ~25% and so forth. Panels B–G show spatial maps whose contrast levels depict the amplitudes of the first six principal components. Note that negative contrast values indicate a time series having an inverse relationship to that shown beneath each spatial map. The illustrated time series represent the extracted temporal behavior occurring in each pixel according to the indicated amplitude. Thus each spatial map identifies a particular time–evolving process of the vascular response that is defined by the indicated time series. The magnitude of each in relation to the total variability is listed below the time series.

Inspection of the first principal component reveals that upon inflation of the pressure cuff, the hemoglobin content in selected areas of the cross section of the arm declines, while other areas (dark regions), notably in the periphery, it increases. We interpret this being associated with collapse of the arterial bed upon occlusion. Following release of the cuff, arterial flow is restored, accompanied by a rapid rise in blood volume. Note that regions with negative contrast values are presumably experiencing the opposite response, *i.e.*, a rapid decrease in blood volume upon restoration of flow. In all, we feel that the indicated phenomenology, and its temporal and spatial response, are entirely consistent with the expected effect of the induced provocation.

Inspection of the maps of the other principal components reveals, in general, a complex temporal response. Note that comparison of between the spatial maps indicates that temporal responses occurring in various regions that appear spatially coincident are notably different. Two other observations deserve emphasis.

The first observation is that even out to the sixth principal component, which comprises only a small percentage of the total spatiotemporal variance, the time series does not appear as random noise. Thus far, we have not tested the statistical significance of these low–amplitude signals. We have, however, performed similar comparisons with dynamic laboratory phantoms experiencing low–amplitude harmonic behaviors and confirmed that correct temporal information is present in components having approximately the same variance. The point is that even though the amplitudes of the components are small, we do not automatically rule them out as having no useful information.

The second observation relates to the time series identified in the fourth principal component. Here we observe that upon inflation of the cuff, a rapid transient rise in hemoglobin levels occurs, followed by a more gradual decline back to baseline. Following this we observe a precipitous decline, followed by an equally precipitous recovery in tissue hemoglobin levels. This is the followed by a second transient rise and subsequent decline to baseline that are precisely coincident with the onset and dissipation, respectively, of reactive hyperemia. In addition, we note with considerable interest that these events are occurring principally in the peripheral regions of the tissue. Despite the apparently small contribution of this principal component to the total variance, we consider these findings entirely plausible. For instance, upon initiation of cuff inflation, some level of venous congestion should occur and this should be most evident in the periphery, where it is found. Next, the gradual return to baseline suggests a redistribution of blood volume, which we also believe likely occurs. Next, the precipitous decline and recovery of tissue hemoglobin levels coincident with release of the cuff is precisely the response one would expect in vessels involved with venous return. Initially upon release, engorged vessels will deflate, perhaps beyond

Figure 5
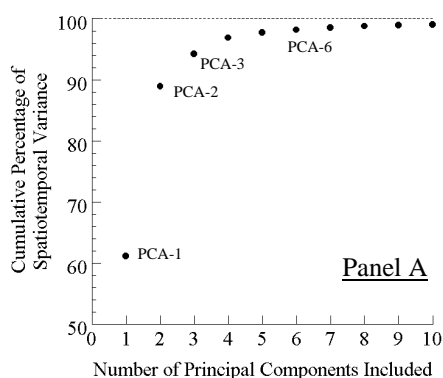
Principal Component Analysis: Reactive Hyperemia. Panel A indicates the cumulative percentage of spatiotemporal variance accounted for by the first M principal components, where $M = 1,\ldots,10$. In panels B–G (next page), the first six normalized principal components (time series) are presented below spatial maps of the amplitude of each response. The indicated gray scale identifies the relative amplitude of the extracted time series in the spatial map.

steady–state levels, and will recover upon full restoration of flow. Finally, as already noted, we observe a hyperemic response occurring in expected spatial regions with the correct temporal sequence.

Panel B   PCA–1   Panel C   PCA–2   Panel D   PCA–3
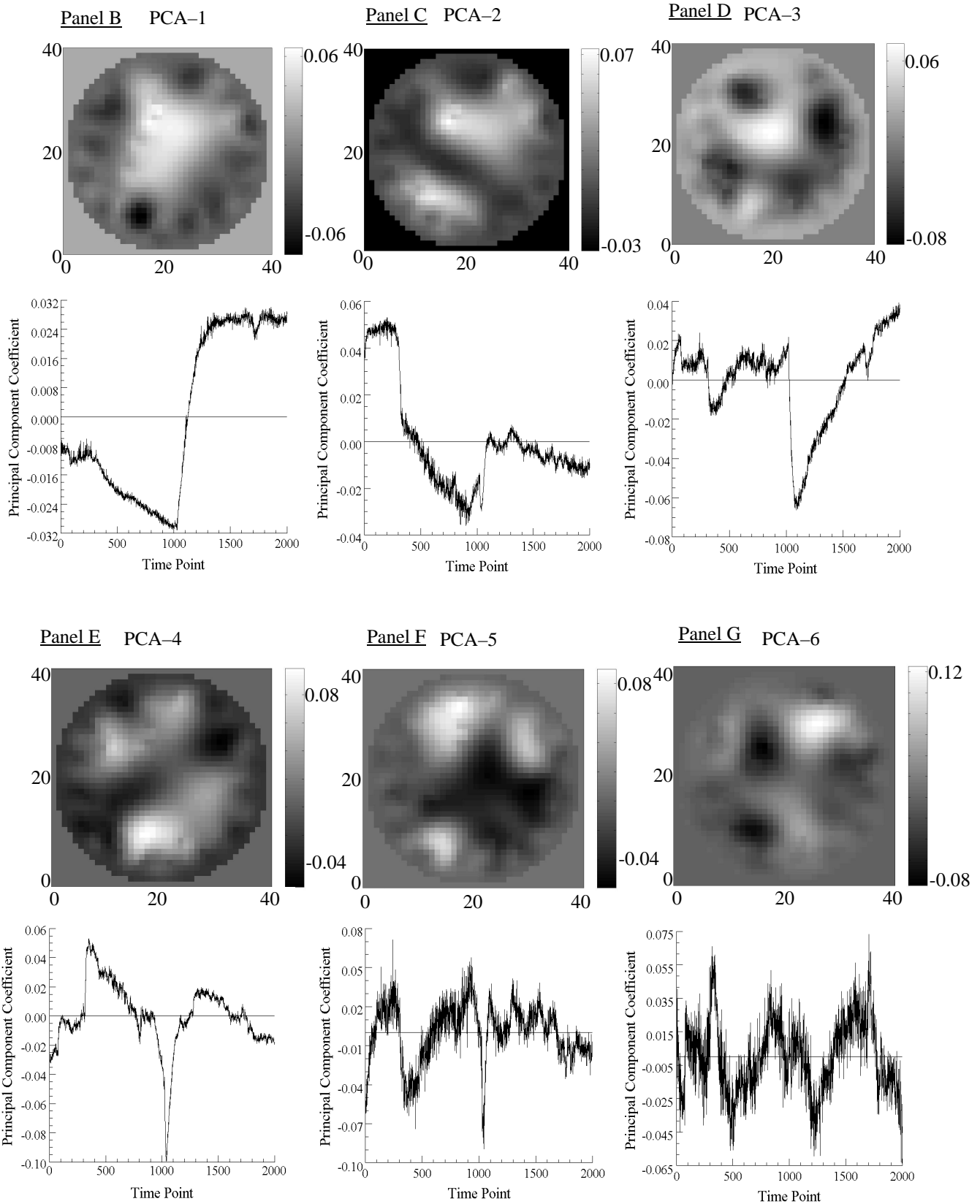
4.3 Long–term System Evolution: Effect of Chronic Tobacco Use

As another example of the value of employing time series studies, we have examined the vascular response to provocation in the forearm of an individual addicted to tobacco compared to a non–smoker. Data in Figure 6 shows time plots of detector responses for a chosen source location. Following an initial rest period lasting approximately 90 sec, 50 mm Hg of cuff pressure was applied to the upper arm, for a period of an additional 90 seconds followed by a recovery period. Inspection shows that compared to the non–smoker, the magnitude of venous congestion is markedly reduced and no evidence of hyperemia is seen. This contrasts the fall in signal levels seen in the non–smoker beginning at approximately time point 650. We interpret this blunted response as consistent with the clinical evidence[20] that chronic tobacco use leads to impairment of the microvasculature.

Figure 6
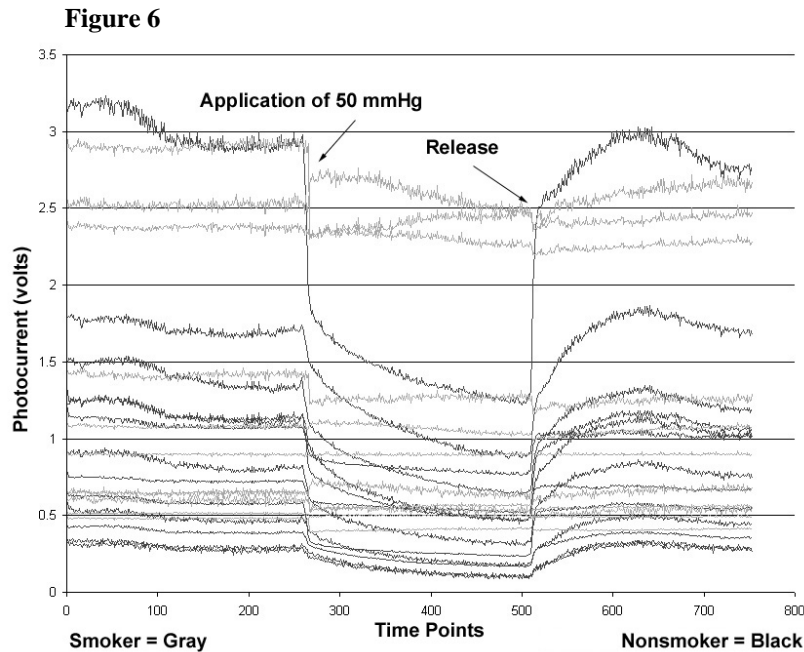
Long–term Response to Chronic Tobacco Use: Detector data (single source) demonstrating attenuation of the vascular response following release of transient arterial inflow reduction.

5. DISCUSSION

The physiologic mechanisms of many clinically observable vascular phenomena are understood only in the grossest ways (*e.g.* vasospastic disorders, reflex sympathetic dystrophy, and reperfusion injury). The underlying global microvascular activities of most vascular phenomena have eluded description, principally due to the lack of appropriate investigational tools. As a general tool, however, optical methods such as photoplethysmography, pulse oximetry, and laser Doppler have been successfully used in many applications to study the vascular response in tissue.[21,22,23] This is possible because hemoglobin is restricted to the vascular compartment. Use of optical methods in a continuous tomographic imaging mode, however, has only recently been considered.[24]

5.1 Dynamic Behavior as a Natural Contrast Agent

In the foregoing series of experiments, we have shown that the dynamic nature of the vascular system, when analyzed using optical methods, can serve as a means of spatial anatomic discrimination. This spatial resolution is accomplished without the use of nephrotoxic intravenous contrast agents, or the use of ionizing radiation. Given that the vascular response is spatially heterogeneous, that the frequency characteristics of the pulsatility of blood flow varies between components of the vascular tree, and that the responses to provocation are dependent on the tissue examined and their expression within the time scales of vascular response, a decomposed description of the individual vascular response in a discrete structure in cross section can be made. Furthermore, a map of the aggregate responses can be generated, describing the global vascular response to a large tissue structure.

5.2 Exploration of Elusive Vascular Pathophysiologic Phenomena

The ability to derive image contrast from temporal features of the vasculature opens the door to exploring a broad range of functional responses that previously have resisted study. For instance, the vascular response to various forms of iatrogenically applied provocation can be examined. These could take the form of simple manipulations such as the use of a pneumatic tourniquet, or the application of vasoactive agents. Here we have examined the phenomenon of reactive hyperemia.[25,26] While the details of the spatial maps and temporal variations reported here require more thorough study, these demonstrations nevertheless provide evidence generally consistent with principal clinical observations. More important, the findings presented provide a basis for developing testable hypothesis of a range of phenomena that have until now eluded detailed examination. Similarly, we believe that by adopting the methods set forth in this report, the examination of non–iatrogenic provocations such as acute or chronic ischemia, trauma, sepsis, or the presence of tumors, all which serve to stimulate a pathologic vascular response, can provide insights that can lead to the development of improved disease detection and monitoring paradigms.

6. ACKNOWLEDGEMENT

7. REFERENCES

[1] M. Nakamura, "Experimental induction of spasm, sudden progression of organic stenosis and intramural hemorrhage in the epicardial coronary arteries," *Basic Research in Cardiology*, **86**(suppl 2), 159–172, (1991).

[2] T. B.Clarkson, R. W. Prichard, and T. M. Morgan, "Remodeling of coronary arteries in human and nonhuman primates," *JAMA* **271**, 289–294 (1994).

[3] U. Hoffman, U. K. Franzeck, and A. Bollinger, "Low frequency oscillations of skin blood flux in peripheral arterial occlusive disease," *Vasa* **23**, 120–124 (1994).

[4] T. M. Griffith, "Temporal chaos in the microcirculation," *Cardiovascular Research* **31**, 342–358 (1996).

[5] D. T. Kaplan and A. L. Goldberger, "Chaos in cardiology," *J. Cardiovascular Electrophysiology* **2**, 342–354 (1991).

[6] W. H. Knapp, C. Dannenberg, B. Marschall, *et al.*, "Changes in local cortical blood flow by neuroactivation and vasoactivation in patients with impaired cognitive function," *Eur. J. Nuclear Medicine*, **23**(8), 878–888 (1996).

[7] J. K. Kanters, M.V. Hogard, E. Agner, N. H. Holstein–Rathlou, "Short– and long–term variations in non–linear dynamics of heart rate variability," *Cardiovascular Research* **31**, 400–409 (1996).

[8] R. L. Barbour, H. L. Graber, Y. Pei, and C. H. Schmitz, "Imaging of vascular chaos," Proc. SPIE 4250 (2001, accompanying report)

[9] H. L. Graber, Y. Pei, and R. L. Barbour, "Imaging of spatiotemporal coincident states by dynamic optical tomography," Proc. SPIE 4250 (2001, accompanying report).

[10] C. H. Schmitz, M. Löcker, J. Lasker, A. H. Hielscher, and R. L. Barbour, "Performance characteristics of a silicon photodiode (SiPD) based instrument for fast functional optical tomography," Proc. SPIE Vol. 4250 (2001, accompanying report).

[11] Y. Pei, "Optical Tomographic Imaging Using Finite Element Method," Ph.D. Dissertation, Polytechnic University, Brooklyn, NY, 1999.

[12] Y. Pei, H. L. Graber, and R. L. Barbour, "Influence of systematic errors in reference states on image quality and on stability of derived information for DC optical imaging," *Applied Optics*, submitted.

[13] C. H. Schmitz, H. L. Graber, H. Luo, I. Arif, J. Hira, Yaling Pei, A. Bluestone, S. Zhong, R. Andronica, I. Soller, N. Ramirez, S.–L. S. Barbour, R. L. Barbour, "Instrumentation and calibration protocol for imaging dynamic features in dense–scattering media by optical tomography," *Applied Optics* **39**, 6466–6486 (2000).

[14] H. L. Graber, C. H. Schmitz, Y. Pei, S. Zhong, S.–L. S. Barbour, S. Blattman, T. Panetta, R. L. Barbour, "Spatio–Temporal Imaging of Vascular Reactivity," in *Medical Imaging 2000: Physiology and Function from Multidimensional Images*, C.–T. Chen, A. V. Clough, Eds., Proceedings of SPIE Vol. 3978, pp. 364–376 (2000).

[15] G. Strang, *Linear Algebra and Its Applications*, 3rd Ed. (Harcourt Brace Jovanovitch, San Diego, CA, 1988)

[16] R. A. Johnson and D. W. Wichern, *Applied Multivariate Statistical Analysis*, 3rd Ed. (Prentice Hall, Englewood Cliffs, NJ, 1992), Chap. 8.

[17] J. Mayhew, D. Hu, Y. Zheng, S. Askew, Y. Hou, J. Berwick, P. J. Coffey, and N. Brown, "An evaluation of linear model analysis techniques for processing images of microcirculation activity," *Neuroimage* **7**, 49–71 (1998).

[18] Y. Zheng, D. Johnston, J. Berwick, and J. Mayhew, "Signal source separation in the analysis of neural activity in the brain," *Neuroimage*, **13**, 447–458 (2001).

[19] L. Zhukov, D. Weinstein, and C. Johnson, "Independent component analysis for EEG source localization in realistic head models," *IEEE Engineering in Medicine and Biology* **19**(3), 87–96 (2000).

[20] I. A. Lehr, "Microcirculatory dysfunction induced by cigarette smoking," *Microcirculation* **7**(6 Pt 1), 367–84 (2000).

[21] H. N. Mayrovitz, "Assessment of the microcirculation: Laser Doppler and transcutaneous oxygen," *J. Vascular Technology* **18**(5) 269–275 (1994).

[22] H. B. Abramowitz, L. A. Queral, W. R. Flinn, *et al.,* "The use of photoplethysmography in the assessment of venous insufficiency: A comparison to venous pressure measurements," *Surgery* **86**, 434 (1979).

[23] P. I. Allen and M. Goldman M, "Laser Doppler Assessment of Skin Blood Flow in Arteriopathic Limbs," *Clin. Phys. Physiol. Meas.* **8** 179–182 (1987).

[24] R. L. Barbour, H. L. Graber, Y. Pei, S. Zhong, and C. H. Schmitz, "Optical tomographic imaging of dynamic features of dense–scattering media," *J. Opt. Soc. Am. A* (2001), in press.

[25] J. M. Van De Water, C. D. V. Indech, and R. B. Indech, "Hyperemic response for diagnosis of arterial insufficiency," *Archives of Surgery* **115**, 851 (1980).

[26] M. I. Cohen and R. L. Vogelzang, "A comparison of techniques for improved visualization of the arteries of the distal lower extremity," *Am. J. Roentgenology* **147** 1021–1024 (1986).